High-Temperature Flexible Transparent Heater for Rapid Thermal Annealing of Thin Films

Renhong Liang,[1] Huizhong Wang,[2] Shu Zhan,[1] Mao Ye[·],[3] Longlong Shu[·],[1,*] Linfeng Fei[·],[1] Danyang Wang[·],[2] Renkui Zheng,[1] and Shanming Ke[·][1,,†]

[1]*School of Materials Science and Engineering, Nanchang University, Nanchang 330031, People's Republic of China*

[2]*School of Materials Science and Engineering, The University of New South Wales, Sydney, New South Wales 2052, Australia*

[3]*Department of Physics, South University of Science and Technology, Shenzhen 518060, People's Republic of China*

Rapid heating is highly sought-after for compositional control in the sintering-annealing process of materials containing volatile elements. Although several innovative approaches have been reported, suitable processes for the rapid annealing of thin films are still very rare. Herein, we develop a high-temperature rapid heating method for thin-film preparation through employing an indium tin oxide (ITO)/mica-based flexible transparent heater (FTH). The ITO/mica FTH shows an extremely fast thermal response (2 s), high saturation temperature ($>830\,°C$), and high heating-cooling rates ($>10^4\,°C\,min^{-1}$). Thermodynamic analysis reveals that the excellent heating performance can be largely attributed to the high heat-transfer coefficient and the low thickness of the mica substrates. The remarkable potential of our ITO/mica FTH for practical use is unambiguously evident by the demonstration of water heating and rapid thermal annealing of ferroelectric oxide thin films.

I. INTRODUCTION

Ceramics and metals are generally sintered-annealed to improve machinability, produce a desired microstructure, or obtain optimal physical properties [1,2]. However, the disadvantages of conventional sintering routes, including relatively low heating rate, long processing time, bulky apparatus, and high cost, greatly impede their wider applications in the preparation of advanced functional materials. The long sintering time is especially problematic in the development of functional ceramics and metal alloys containing highly volatile elements, such as Li, Na, Pb, and Bi. To address the aforementioned issues, some innovative sintering technologies allowing rapid heating (RH) were developed in recent years. Hu and co-workers [3] proposed a carbothermal shock method for alloying multiple immiscible elements into single-phase nanoparticles. Another process, named flash joule heating (FJH), reported by Tour and co-workers [4–6], can turn bulk quantities of carbon sources into graphene flakes in milliseconds. FJH can also be generalized to produce other two-dimensional

(2D) nanoflakes efficiently. In addition to rapid thermal processing of nanoparticles and nanoflakes, ultrafast high-temperature sintering using two joule-heating carbon strips has also been tailor-made for ceramic fabrication recently [7]. In a nutshell, these RH technologies feature a uniform temperature distribution, high heating-cooling rates (up to $10^4\,°C\,min^{-1}$) and a high heating temperature (up to $3000\,°C$). The whole sintering process of RH technologies can be completed in a few seconds, far outpacing those of conventional furnaces. However, these RH techniques are not suitable for the preparation of thin-film materials, especially for epitaxial growth. Here, we develop a high-temperature rapid heating method for the growth of epitaxial thin films through employing a flexible transparent heater (FTH) with ultrafast thermal response.

Flexible and transparent heaters find their applications in broad areas, including defogging and deicing of glass that is used typically in liquid-crystal display panels, vehicles, avionics, etc. [8,9], ensuring the fast response of electronic devices under extreme environmental conditions, heating of sensors and microchannels [10–12], and so on. A FTH generally consists of a transparent conducting electrode (TCE) on a flexible transparent substrate. Meanwhile, the

---

*llshu@ncu.edu.cn

†ksm@ncu.edu.cn

TCE is an essential component of many optoelectronic devices, such as solar cells, light-emitting diodes, touch-screens, and displays, in which there are different active layers on the TCE [13]. Annealing is often needed to crystallize the layers and enhance the coupling between active layers and the TCE. Rapid heating is critical when highly volatile elements are present in these active layers. Because of the high conductivity of TCEs, joule heating, instead of external heating, in these devices is possible. Joule heating is advantageous in the sense that no external heat source would be required. On the other hand, joule heating would offer high performance or additional functionality for devices with FTHs. For instance, a VO_2-based thermal camouflage or thermochromic device could render a faster response when combined with a high-performance transparent heater [14,15].

To date, neither the heating temperature nor thermal response rate of the reported FTHs are impressive yet. The polymer-based FTHs are not well suited for rapid heating because of their low heating temperature and slow thermal-response rate, which are related to their low melting point and low thermal conductivity [16]. A metal-nanofiber (MNF) network heater is proved to have a maximum heating temperature higher than 800 °C. But the best heating rate of the MNF is only 10^3 °C min^{-1}, which is not sufficient for rapid heating [17]. The short life-time or poor thermal stability arising from the oxidation of metal nanofibers at elevated temperatures is another down-side of MNF-based heaters. In our previous work [18], a FTH with ultrafast thermal response (<3 s) was achieved by using an all-inorganic Al-doped ZnO (AZO) TCE grown on layered mica substrate. However, the operating temperature of the AZO/mica heater could not exceed 400 °C, limiting its capacity in rapid heating. Here, we report a highly transparent and flexible heater possessing a simultaneous ultrahigh heating temperature and super-fast response by using indium tin oxide (ITO)/mica het-eroepitaxy, for which excellent transparency in the visible and near-infrared regions and the low sheet resistance of ITO/mica heterostructures have been documented before [19]. Our ITO/mica heater can reach a heating temperature of >830 °C with a response time of 2 s, outperforming all the existing FTHs. To evaluate the effectiveness of such a FTH for rapid heating, the *in situ* annealing of amorphous Pb(Zr, Ti)O_3 (PZT) thin film is conducted. To extend this study, BaTiO$_3$ (BTO), and Hf$_{0.5}$Zr$_{0.5}$O$_2$ (HZO) amorphous films without any volatile element are also annealed by FTH. These ferroelectric oxide thin films can be swiftly crystalized using our thin-film RH technique, as evidenced by their decent ferroelectric properties. Our work will not only enrich the family of flexible transparent heaters but also potentially create a pathway to prepare high-quality functional thin films through a facile and cost-effective rapid-heating strategy.

II. EXPERIMENTAL DETAILS

The ITO film is deposited on freshly cleaved mica via a pulsed laser deposition (PLD) system equipped with a KrF excimer laser with a wavelength of 248 nm using a commercial ITO (90% In$_2$O$_3$ and 10% SnO$_2$) target. The surface dimensions of the substrates are 15×15 mm^2. The thickness of the substrates should be lower than 100 μm to enable flexibility and better heat transfer. No surface treatment and precleaning of the mica substrate is required prior to deposition. The deposition chamber is initially evacuated to a base pressure of 10^{-6} Torr. In the deposition process, the energy density and repetition rate of the pulsed laser are about 1.5 J cm^{-2} and 10 Hz, respectively. A buffer layer of yttria-stabilized zirconia (YSZ) about 3 nm in thickness is first deposited on mica at a substrate temperature of 400 °C under 0.1 mTorr oxygen pressure, and then the ITO film is deposited at a substrate temperature of 300–500 °C under 0.1–200 mTorr oxygen pressure. After the deposition process, the ITO films are annealed in a growth chamber at 500 °C for 0–30 min under an oxygen pressure of 10 mTorr followed by cooling to room temperature at a rate of 20 °C min^{-1}.

The crystal structure and epitaxial relationship are investigated by using a Rigaku Smart-lab x-ray diffractometer with monochromatic Cu $K\alpha 1$ radiation ($\lambda = 1.54056$ Å). The cross-section TEM specimen is prepared by the focused ion beam (FIB) technique. The TEM specimen is then examined on a Tecnai G2 F20 S-Twin instrument working at an acceleration voltage of 200 kV. Images of the surface morphology of the ferroelectric films are obtained using a scanning electron microscope (SEM, SU-70, Hitachi).

The sheet resistances of the films are characterized by the standard four-point-probe method. Five different areas on the ITO film are measured to get the average sheet resistance. The transmission spectra are recorded on a spectrophotometer (Shimadzu, UV-2450). Electrical polarization studies are carried out on a Cypher ES (Asylum Research) atomic force microscope. Detailed polarization maps are generated in dual AC resonance tracking piezoresponse force microscopy (PFM) mode by using Ir/Pt-coated conductive tips (Oxford, ASYELEC.01-R2).

Profiles of temperature are measured with a K-type thermocouple thermometer and an infrared camera (E40, FLIR system) simultaneously (see Fig. S1 within the Supplemental Material [20]). The temperature measurements are performed in a dry room with controlled room temperature. The Ag (50 nm) layer with a width of 2 mm is deposited at two edges of the ITO to apply the voltage. Metal wires are glued to the Ag electrodes by using high-temperature conductive silver paint (SPI supplies, working temperature up to 900 °C). Meanwhile, the ITO/mica heater is supported by metal wires, so there is only heat exchange with the air. The dc voltage is applied by a dc power supply

(KXN-3030D), which can also record the current of the heaters.

III. RESULTS AND DISCUSSION

A. Structural, optical and electrical characterization

Mica is a well-known naturally occurring transparent crystalline material and a promising substrate for the van der Waals (vdW) epitaxial growth of transparent conductive oxide films [21–24], owing to its good flexibility, surface flatness at the atomic level, high thermal stability, as well as high-temperature tolerance of up to 1200 °C [25]. Here, both muscovite (operation temperature >600 °C) and fluorphlogopite (operation temperature >1000 °C) are used as flexible transparent substrates for the deposition of ITO. A YSZ buffer layer is first deposited to ensure epitaxial growth of ITO [26,27]. High-resolution x-ray diffraction (XRD) is carried out to determine the crystallographic orientation of the heteroepitaxial structure. As shown in Fig. 1(a), the observation of only {222} peaks of ITO on the mica (00l) plane suggests the c-axis orientation of the ITO film without any secondary phase, and the diffraction peaks denoted by asterisks correspond

to the mica (00l) planes that are parallel to its cleavage plane. The off-axis φ scan is used to further identify the in-plane structural relationship in the heterostructure. As shown in Fig. 1(b), the mica substrate shows a threefold symmetry with three {202} peaks at 120° intervals, while the ITO film exhibits six {440} peaks with 60° intervals, which indicate the multidomain structure existing in the ITO films on mica. The epitaxial relationship between ITO and mica can be determined as $(222)_{\text{ITO}}\|(001)_{\text{mica}}$ and $[\bar{1}10]_{\text{ITO}}\|[010]_{mica}$. The rocking curve around the ITO (222) reflection exhibits a full width at half maximum (FWHM) of 0.85°, indicating the good crystallinity of ITO films [Fig. 1(c)]. Symmetric and asymmetric reciprocal space mapping (RSM) are performed and taken around the (222) [Fig. 1(d)] and (626) (Fig. S2 within the Supplemental Material [20]) reflections of the ITO film, respectively. Derived from the RSM result, the in-plane reciprocal distance can be calculated as 1.167 Å, and the in-plane lattice constant is 10.171 Å, indicating a bulklike lattice parameter. In addition, the ITO (222) peak position of the films grown on mica are very close to the hypothetical bulk ITO value, also suggesting that this film is fully relaxed.
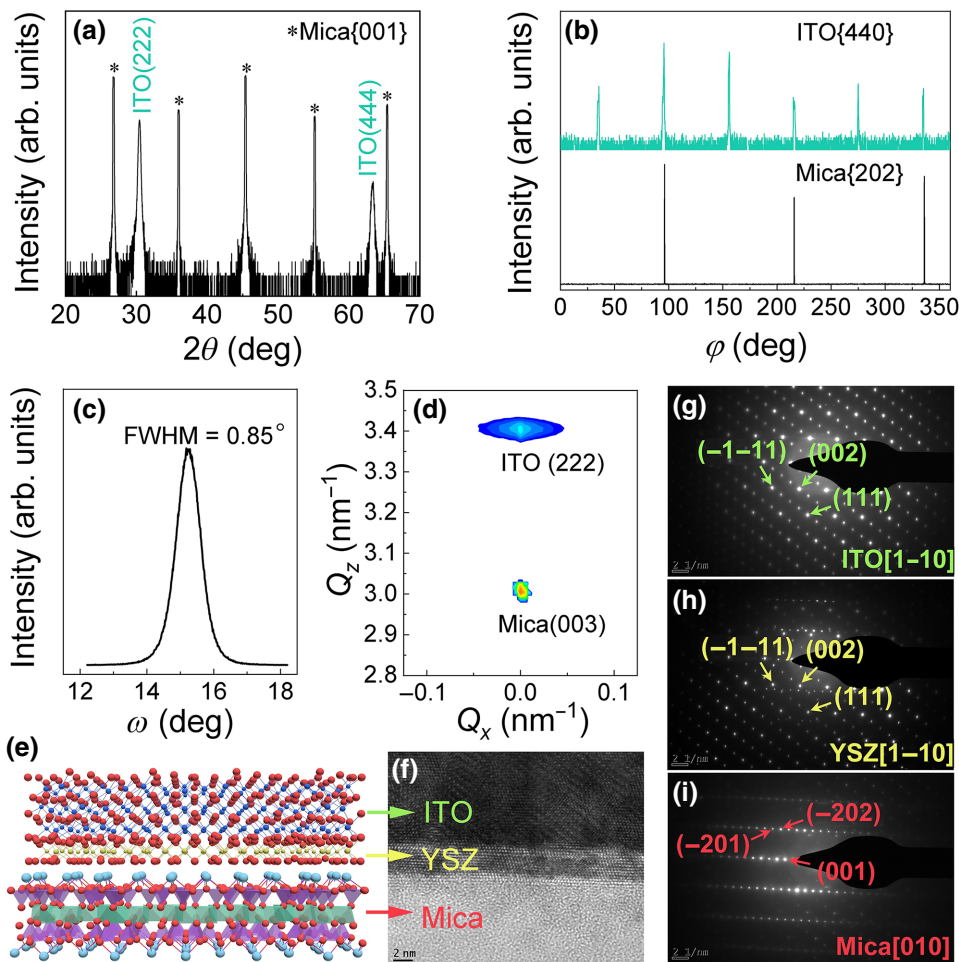

FIG. 1. Structural characterizations of ITO/YSZ/mica (muscovite) heteroepitaxy. (a) Typical $2\theta/\omega$ scan of ITO/YSZ/mica. (b) φ scans at ITO {440} and mica {202} diffraction peaks. (c) Rocking curve of the (222) peak of ITO film. (d) Reciprocal space mapping round the ITO (222) reflection. (e) Schematic of the ITO/YSZ/mica heteroepitaxy structure. (f) Cross-section TEM image of ITO/YSZ/mica. Selected-area electron diffraction patterns of (g) mica, (h) YSZ, and (i) ITO layer.

To characterize the detailed microstructure of the ITO/YSZ/mica heterostructure, transmission electron microscopy (TEM) is employed. As shown in Fig. 1(f), a cross-section TEM image shows the flat interfaces of ITO/YSZ and YSZ/mica. The thickness of the YSZ buffer layer is about 3 nm. The corresponding selected-area electron diffraction (SAED) patterns of the heterostructure are shown in Figs. 1(g)–1(i). The reciprocal lattices of mica, YSZ, and ITO are clearly indexed and in good agreement with the epitaxial relationship confirmed by the XRD results.

On account of the excellent structural quality, outstanding optical and electrical properties of the ITO/YSZ/mica heterostructure are expected. Figure 2 compares the sheet resistance (R_s) and optical transmittance of ITO thin films that are deposited under selected oxygen pressures [Fig. 2(a)] and at various substrate temperatures [Fig. 2(b)]. It is evident that low sheet resistance and high transparency can be achieved when the ITO thin films are grown under 10 mTorr oxygen pressure and at substrate temperature of 300 °C. The annealing conditions

and film-thickness-dependent sheet resistance and optical transmittance of ITO films deposited on muscovite are provided in Fig. S3 within the Supplemental Material [20]. The electronic conduction properties of ITO thin films demonstrate marked free-carrier-like characteristics. The conductivity of ITO films is generally affected by the electron concentration, which depends on Sn doping and oxygen vacancies, and the mobility of free electrons, which depends on the crystallinity, strain state, and defect density of ITO. In a typical PLD process, the content of oxygen vacancies can be tuned by varying the oxygen pressure, annealing temperature, time, etc. Obviously, high-quality transparent conductive ITO thin films can be obtained when processed under optimal conditions. The typical sheet resistance of a 500-nm-thick ITO film is as low as 7 Ω sq^{-1} with an average transmittance of 90.8% (visible wavelength), both of which are considerably better than those of ITO grown on conventional flexible substrates. To compare the electrical and optical properties of different samples, a figure of merit (FOM) [28,29], which is defined as $\emptyset_{TC} = T_{tran}^{10}/R_s$ (T_{tran} represents the average
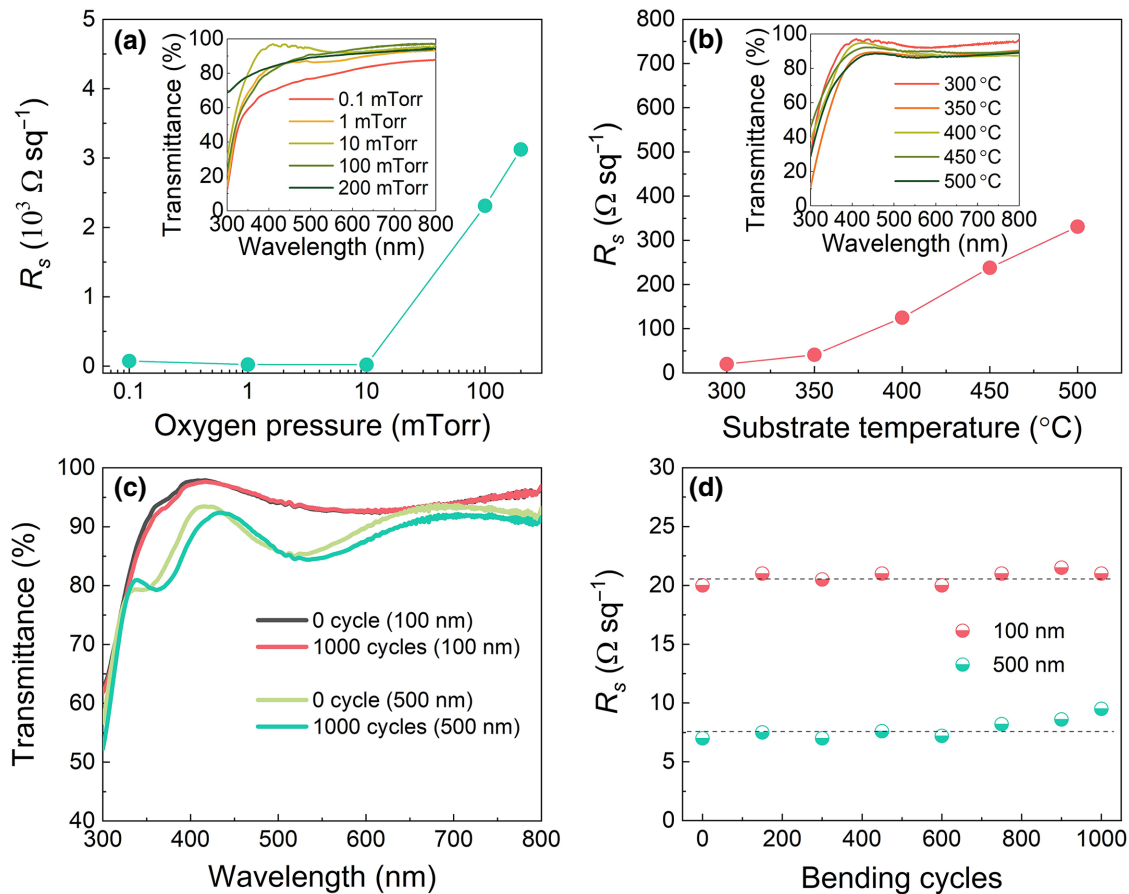

FIG. 2. Optical, electrical, and mechanical characterization of the ITO/mica (muscovite) FTH. (a),(b) Sheet resistances as a function of oxygen pressure and substrate temperature, respectively. Insets present the transmittance of the ITO films at wavelengths of 300–800 nm. (c) Transmittance and (d) sheet resistance of ITO/mica heteroepitaxy at selected thicknesses before and after the bending test.

TABLE I. FOM value as a function of ITO film thickness. These films are deposited on muscovite at a base pressure of 10 mTorr with a substrate temperature of 300 °C.

Thickness (nm)	Average transmittance (T, %)	Sheet resistance ($\Omega\,\mathrm{sq}^{-1}$)	FOM ($10^{-3}\,\Omega^{-1}$)
100	94.6	20	28.8
200	92.4	15	30.2
300	91.9	13	33.4
400	91.7	12	35.2
500	90.8	7	54.4

transmittance at visible wavelength), is considered. Table I shows the ITO thickness dependence of the FOM. A high FOM of 54.4 is obtained for a 500-nm-thick ITO film grown on muscovite, representing a high value among the ITO layers deposited on conventional flexible substrates reported to date. By replacing muscovite substrate with fluorphlogopite, the optical and electrical properties of the ITO films will be further improved, as discussed in the next section.

It is widely reported that the vdW heteroepitaxial thin films prepared on mica possess superior thermal stability and mechanical flexibility [18,19,21–24,30]. To verify the stability against mechanical bending of our ITO films on mica, a very rudimentary cyclic bending test is performed (Fig. S4 within the Supplemental Material [20]). Figures 2(c) and 2(d) show the optical transmittance and sheet resistance of 100- and 500-nm-thick ITO thin films, respectively, after cyclic bending for 1000 cycles with a bending radius of 5 mm. The transmittance and sheet resistance of ITO/mica remain almost constant during the bending test, confirming excellent bending fatigue endurance and the robustness of these heterostructures.

B. Joule heating behavior

Given their exceptional flexibility and conductivity, our ITO/mica heterostructures are ideal candidates for flexible heaters. For a thin-film heater [Fig. 3(a)], heat is generated through the joule heating effect of the TCE and transferred to the substrate by conduction. On the other hand, some of the generated heat will dissipate into the air through convection and radiation from both surfaces. Eventually, the temperature of the FTH is saturated when joule heating and dissipation reaches an equilibrium state. Figures 3(b) and 3(c) show the time-dependent surface temperatures of the ITO/mica-based heater with different sheet resistances of 20 and 6 $\Omega\,\mathrm{sq}^{-1}$, respectively, at different driving voltages (2–18 V). The steady saturation temperature (T_s) in both cases increases with increasing driving voltage. At any given driving voltage, a higher T_s is obtained for a heater with a low resistance. For instance, a T_s of 540 °C is achieved at 18 V for the ITO/mica heater with a sheet

resistance of 20 $\Omega\,\mathrm{sq}^{-1}$, whereas a significantly higher T_s of 840 °C is obtained at the same applied voltage for the 6 $\Omega\,\mathrm{sq}^{-1}$ heater. Impressively, both ITO/mica heaters can reach their respective T_s within 3 s, regardless of the driving voltage and sheet resistance (see also Videos S1 and S2 within the Supplemental Material [20]). This implies that the thermal-response time, defined as the time required to reach 90% of the saturation temperature, is nearly independent of the power supply and conductivity of the TCE. The extremely fast thermal response of our ITO/mica FTH is further evidenced by the heating- and cooling-rate curves [Fig. 3(d)], calculated from the first-order derivative of the time-dependent temperature curve. It is observed that the ITO/mica heater displays a high heating rate of 220 °C s^{-1} (1.32 × 10^4 °C min^{-1}) and a slightly lower cooling rate of 180 °C s^{-1} at 18 V, both of which are satisfactory for the application of rapid heating.

To comprehensively understand the mechanism behind this remarkable heating behavior of our ITO/mica FTH, thermodynamic analysis is conducted. In principle, the input energy of joule heating (P) equals the sum of the energy stored in the heater and the power losses through convection (Q_c) and radiation (Q_r) [31–33]:

$$P = \frac{V^2}{R} = (C_1 + C_2)\frac{dT}{dt} + (Q_c + Q_r), \qquad (1)$$

where C, T, and t are the heat capacity, temperature of the heating system, and time, respectively; subscript 1 refers to the conductive film and 2 to the substrate. V and R are the applied voltage and the resistance of the conductive film, respectively. Generally, the convective heat loss can be expressed as [33]

$$Q_c = Ah_c(T - T_0), \qquad (2)$$

where h_c is the convective heat-transfer coefficient; T_0 is the initial surface temperature. The radiative heat loss is expressed by the Stefan-Boltzmann law [34–36]:

$$Q_r = \varepsilon\sigma A(T^4 - T_0{}^4) = Ah_r(T - T_0), \qquad (3)$$

where ε is the surface emissivity, σ is the Stefan-Boltzmann constant, A is the surface area, and h_r is the temperature-related radiation heat-transfer coefficient. ITO film has a low surface emissivity of 0.21 at room temperature, while the value of mica is 0.75. It should be noted that their surface emissivity will vary with temperature, in particular, at high temperatures, leading to a temperature-dependent h_r.

As suggested by Ye and co-workers [36], we can take a temperature independent h_r, i.e., a constant h ($h = h_r + h_c$), to solve the differential equation for an approximate analysis. The temperature of the heater is described by the
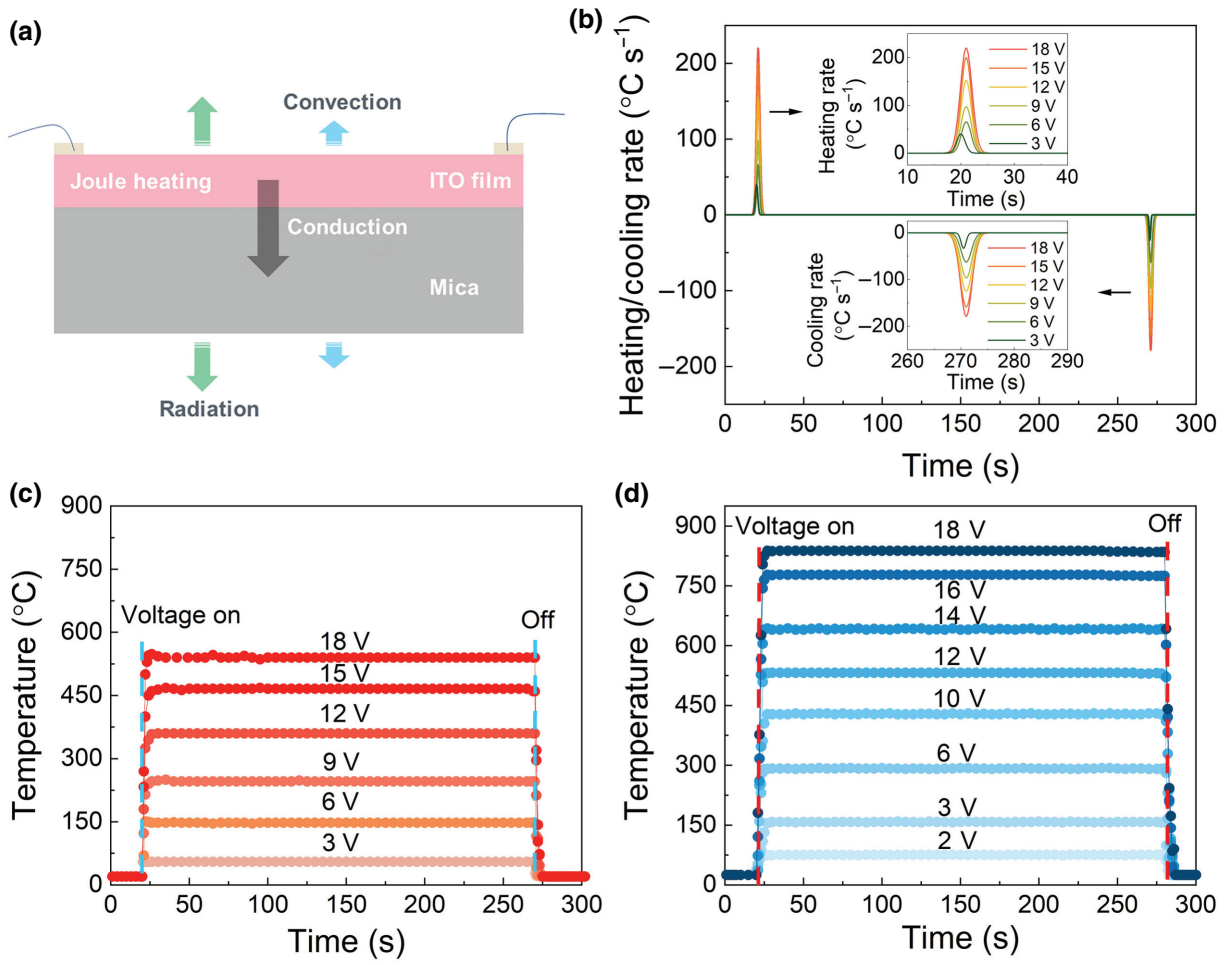
FIG. 3. (a) Schematic of heat transfer in an ITO/mica FTH. Heat dissipates into the air mainly through convection and radiation from both surfaces. Temperature profiles of an ITO/mica FTH with different sheet resistances of (b) $20\ \Omega\,\mathrm{sq}^{-1}$ and (c) $6\ \Omega\,\mathrm{sq}^{-1}$, where the substrate thickness is fixed at 100 μm. (d) Heating and cooling rates of the $20\ \Omega\,\mathrm{sq}^{-1}$ ITO/mica heater at selected input voltages. Heating- and cooling-rate curves are smoothed for clarity.

solution of Eq. (1),

$$T = T_0 + \frac{V^2}{RhA}[1 - \exp(-t/\tau)], \tag{4}$$

$$\tau = \frac{C_1 + C_2}{hA} = \frac{m_1 c_1 + m_2 c_2}{hA} \approx \frac{m_2 c_2}{hA} = \frac{\rho_2 c_2 d_2}{h}, \tag{5}$$

$$T_s = T_0 + \frac{V^2}{RhA} = T_0 + \frac{P}{hA}, \tag{6}$$

where m, c, ρ, and d are the mass, specific heat capacity, density, and thickness of the substrate, respectively. τ depicts the time constant of the transient thermal response and determines the response time. Due to the small thickness of ITO (100 nm) compared to that of the substrate (25–100 μm), the heat capacity of ITO film can be neglected, and the heat capacity of the substrate dominates the transient process of the heating system, as revealed by Eq. (5). This explains why the response time does not vary

with the applied voltage and resistance of ITO, as shown in Figs. 3(b) and 3(c).

Figure 4 illustrates the substrate-thickness dependence of the heating temperature, which can be well fitted to Eq. (4). The fitted time constants (inset of Fig. 4) linearly increase with the thickness of the substrate. The very low time constant (e.g., 1.18 s for 25-μm mica and 2.86 s for 100-μm mica) quantitatively explains the ultrafast thermal response of our ITO/mica heater. In marked contrast, the time constant is 73 s for a graphene/glass heater [31], 42 s for a commercial ITO/glass heater (see Fig. S5 within the Supplemental Material [20]), and 25 s for an Ag nanowire heater with a 150-μm polyethylene terephthalate (PET) substrate [36]. By using values of the material parameters in Table II, the heat-transfer coefficient, h, of mica is found to be 51 $\mathrm{W\,m^{-2}\,K^{-1}}$, which is much larger than those of PET (12 $\mathrm{W\,m^{-2}\,K^{-1}}$) [37] and glass (11 $\mathrm{W\,m^{-2}\,K^{-1}}$) [31]. Therefore, according to Eq. (5), the small time constant observed for the mica-based FTH should be mainly
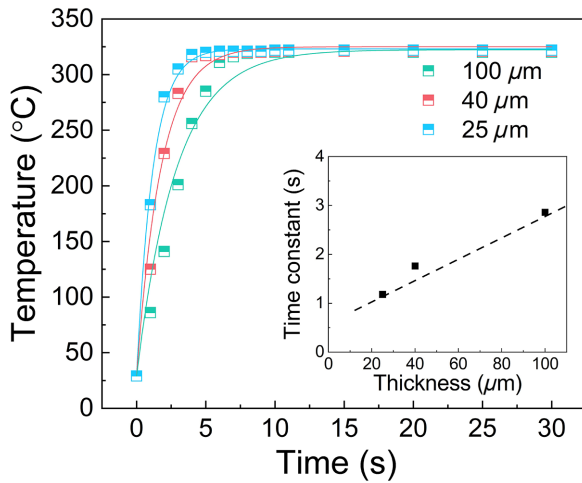
FIG. 4. Substrate-thickness-dependent time-temperature curves for an ITO/mica (muscovite) FTH with selected substrate thicknesses. Solid lines are the best-fitting curves according to Eq. (4). Inset shows the corresponding time constant t, which linearly increases with the thickness of substrate.

attributed to the high heat-transfer coefficient (h) and low thickness (d_2) of the mica substrate. Most importantly, the thickness of a thin mica plate can be more readily lowered to several microns, and even several nanometers, through mechanical exfoliation [38], thus further reducing the thermal-response time and benefiting the applications of rapid heating and cooling.

As seen from Eq. (6), the saturation temperature of a heater is linearly dependent on the input power, regardless of the heater resistance. In this case, all the data points on the plot of the saturation temperature versus input power for the ITO/mica heater with different resistances should be collapsed into a single master curve, i.e., a straight line. As shown in Fig. 5(a), however, the T_s-P plot starts to deviate from a linear relationship when T_s is higher than 300 °C, suggesting that the radiative heat-transfer coefficient, h_r, can no longer be considered as a constant at elevated temperatures but manifests a strong temperature dependence. Previous reports [39–42] on different types of heaters have

demonstrated that the radiative heat loss is negligible when $T_s < 200$ °C. Considering the temperature-dependent surface emissivity of ITO [43,44] and mica [45] (see Fig. S6 within the Supplemental Material [20]), the radiative heat loss is evaluated according to the Stefan-Boltzmann law and plotted in Fig. 5(b). In the low-temperature region up to 300 °C, radiative heat loss is in the order of 10^{-3} to 10^{-2} W cm^{-2}, which is much lower than the input power density. Therefore, radiative heat loss is negligible in this temperature range and the assumption of a temperature-independent h_r is viable. When $T > 300$ °C, radiative heat loss rises rapidly and nonlinearly. The calculated radiative heat loss at 800 °C is 3.13 W cm^{-2}, which is comparable to the input power density. The substantial radiative heat loss at high temperatures is responsible for the observed nonlinear T_s-P behavior in Fig. 5(a).

Despite the large radiative heat loss, an extremely high heating temperature of 830 °C with a short thermal-response time of 2 s is realized using our ITO/mica flexible transparent heater. Retention [Fig. 6(a)] and repeated heating tests [Fig. 6(b)] result in a nearly unchanged saturation temperature, T_s, versus time or cycling number, indicating excellent stability and the reproducibility of this heater. Figure 6(c) summarizes the key performance parameters of some transparent heaters based on various materials, such as crackle mesh [46], metal nanowires (NWs) [40,47–51], graphene [31,37,52–54], carbon nanotubes [55–59], and metal-oxide thin films [18,60,61]. Compared to these heaters, our ITO/mica shows an extremely fast thermal response (3 s), high saturation temperature (840 °C), and high heating-cooling rates ($>10^4$ °C min^{-1}).

C. Applications of ITO/mica FTH for rapid heating

Applications of the high-performance ITO/mica heater in water heating and rapid thermal annealing of functional oxide thin films are demonstrated in this work. The excellent heating capability of the ITO/mica heater in a bent state is illustrated in Figs. 7(a)–7(d). An ITO/mica FTH with very good flexibility and transparency [Fig. 7(a)] can be attached tightly to the side wall of a glass beaker with a radius of 12.5 mm [Fig. 7(b)]. Optical transparency is

TABLE II. Key properties of the substrates for transparent heaters.

Substrate materials	Thermal conductivity (W m^{-2} K^{-1})	Specific heat capacity (c, J g^{-1} K^{-1})	Density (ρ, g cm^{-3})	H (W m^{-2} K^{-1})	τ (s)
PET	0.15	1.28	1.38	12[a]	50
Glass	1.39	0.89	2.21	11[b]	73
Muscovite	3.3	0.871	2.77	51	1.18[c]
Fluorphlogopite	3.75	0.836	2.78	55	1.05[c]

[a]Reference [37].
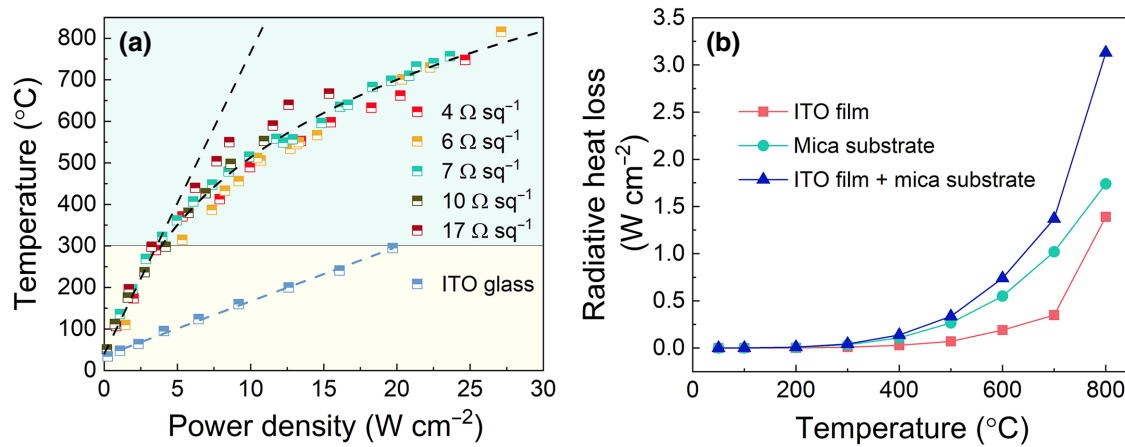[b]Reference [31].
[c]The thickness of the substrate is 25 μm.

FIG. 5.   (a) Saturation temperature versus electrical power density of the ITO/mica (fluorphlogopite) FTHs with different sheet resistances. Data for commercial ITO/glass are also provided for comparison. (b) Theoretical radiative heat power loss of ITO film and mica substrate surfaces as a function of temperature. (Values of surface emissivity used can be found in Fig. S6 within the Supplemental Material [20].)

still preserved for the glass beaker after the attachment of the thin-film heater. Heat generated by the FTH can be efficiently transferred to water in the beaker. The temperature of water (10 ml) rises from room temperature to 100 °C in about 75 s, as shown in Figs. 7(c) and 7(d). A defogging test is also carried out to signify the ultrafast response of our ITO/mica FTH in a more straightforward manner. Recovery of the transparency of the fogged glass is completed within 2 s through applying a voltage of 6 V, as shown in Fig. S7 within the Supplemental Material [20]. This highly efficient defogging and defrosting capability is needed for automotive windscreens and windows.

The ultrafast heating-cooling rates enabled by our FTH [see Figs. 3(b) and 3(c)] are highly attractive for crystalizing thin films compared with those of other sintering methods, such as rapid thermal annealing (RTA) [62]. RTA often relies on costly equipment and offers a mediocre heating rate of about 10^3 to 10^4 °C min^{-1}. Furthermore, the ITO/mica itself can serve as a substrate with a bottom electrode and both sides of the FTH are available for deposition [Fig. 7(e)]. Commonly studied ferroelectric oxide thin films, including PZT, BTO, and HZO, are selected as the model systems to verify the feasibility and effectiveness of our ITO/mica FTH in the rapid thermal processing of thin films.
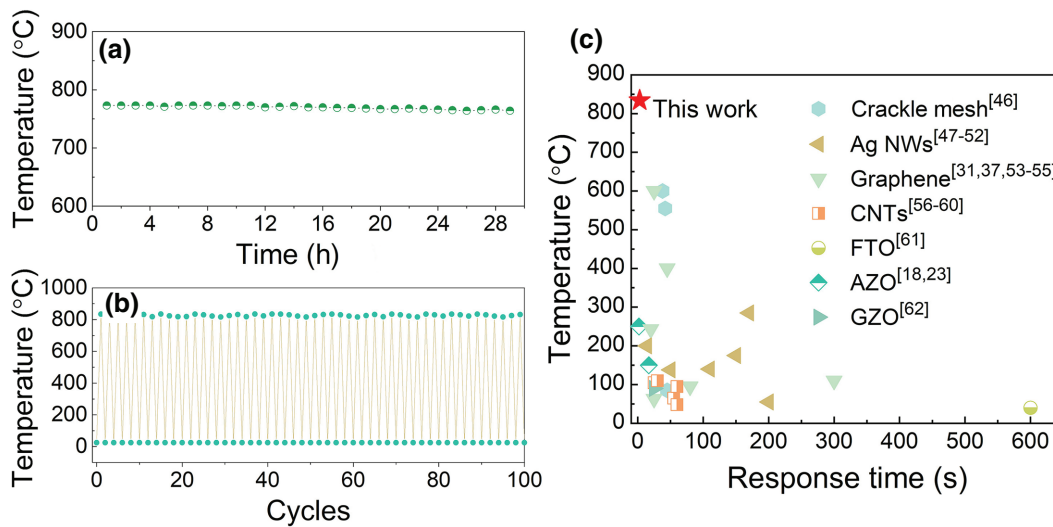

FIG. 6.   (a) Time-dependent temperature profile of ITO/mica (fluorphlogopite) FTH with a sheet resistance of 6 Ω sq^{-1} at 16 V. (b) Heating and cooling cycles of a ITO/mica (fluorphlogopite) FTH with a sheet resistance of 8 Ω sq^{-1} at 28 V. (c) Comparison plot of saturation temperature achieved versus response time for various flexible heaters.
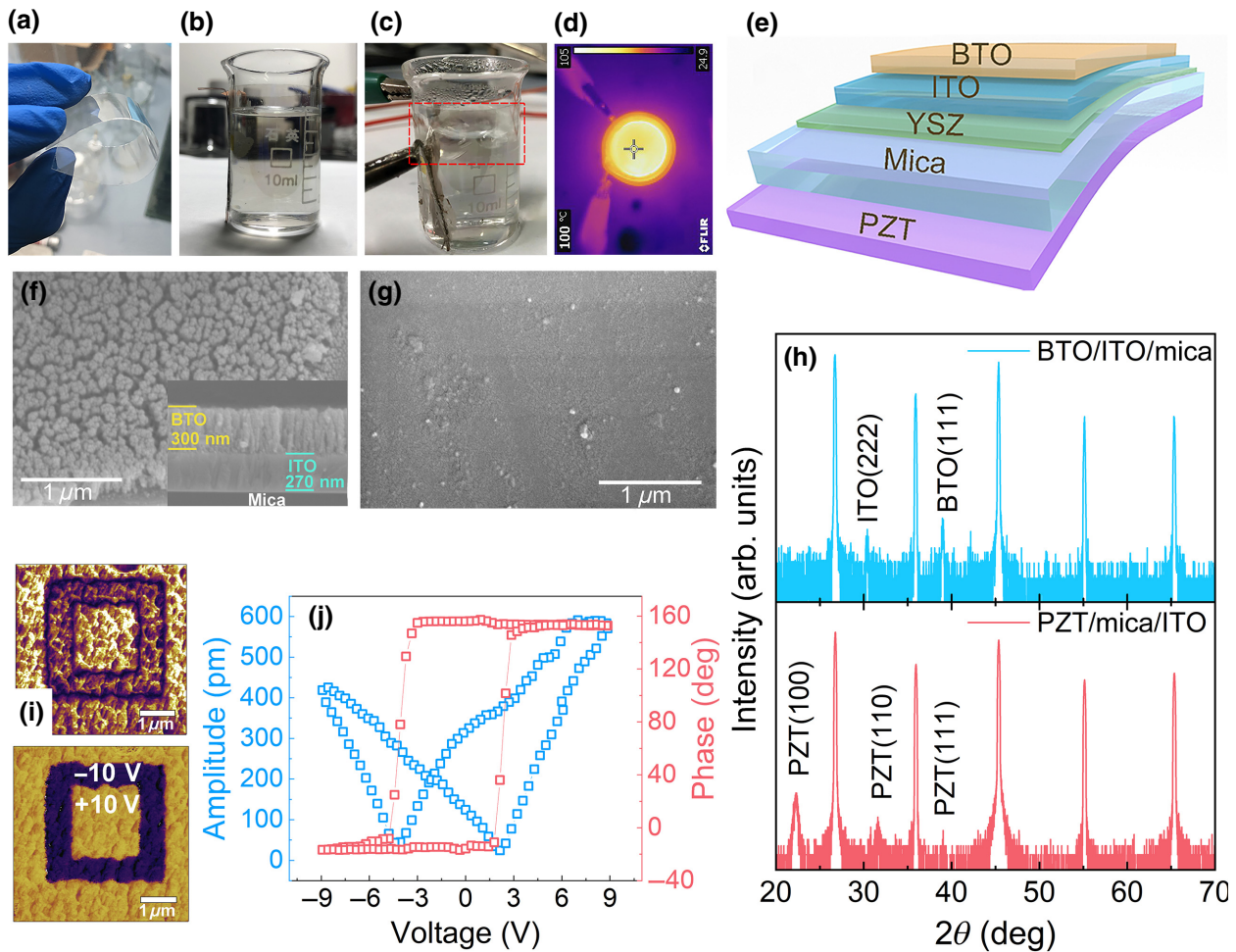
FIG. 7. Applications of ITO/mica (fluorphlogopite) FTH for rapid heating. (a)–(d) Demonstration of the performance of ITO/mica FTH by heating a beaker filled with 10 ml of water. (e) Schematic of the reusable *in situ* annealing furnace, where both sides of the FTH can be used for thin-film deposition and annealing. (f),(g) SEM images of the surfaces of the amorphous and *in situ* annealed BTO films, respectively. Inset of (f) shows the corresponding cross-section image. (h) XRD patterns of the *in situ* annealed BTO and PZT thin films, where BTO is deposited on the ITO surface and PZT is deposited on the mica surface. (i) PFM amplitude and phase images of the annealed BTO film. (j) Local PFM hysteresis loops of the annealed BTO film.

The amorphous oxide thin films are first deposited on either the ITO side or the mica side at room temperature by PLD. The SEM image of an amorphous BTO film in Fig. 7(f) displays clearly an uncompacted structure with many submicron-scale cracks. After rapid annealing by the FTH, the BTO film becomes dense [Fig. 7(g)] and well crystallized with a preferred (111) orientation [Fig. 7(h)], while the PZT film exhibits a polycrystalline perovskite structure, since it is deposited on the back surface of mica. Excellent ferroelectric properties of the FTH-processed BTO, PZT, and HZO films are confirmed by PFM results, as shown in Fig. 7 and Fig. S8 within the Supplemental Material [20]. Most importantly, the films grown on the back side of mica can be exfoliated and transferred to other substrates by a simple mechanical exfoliation technique

[63–66], due to the 2D layered structure of mica. Herein, the ITO/mica heater could be a reusable "*in situ* annealing furnace" for thin-film crystallization.

Here, the ITO/mica vdW heteroepitaxy is fabricated by PLD, which is a successful method for obtaining high-quality epitaxial films of oxides. PLD has the advantage of variable process parameters, such as substrate temperature and rate of deposition (as determined by the energy per pulse), and the repetition rate makes the deposition process more flexible and effective. PLD also provides the stoichiometric transfer of material from the target to the substrate, and thereby, ensures better stoichiometric control. However, despite great progress in recent years [67–70], large-scale fabrication is still a big challenge for PLD. Fortunately, vdW epitaxy (e.g., ITO) on mica can

also be achieved by magnetron sputtering, which is commercialized in large quantities for large-size productions (up to 12 in.).

IV. CONCLUSION

The vdW epitaxial growth of high-quality transparent conducting ITO thin films is successfully achieved on YSZ-buffered flexible transparent mica substrates. The ITO/mica heterostructure not only retains the superior transparency and flexibility of mica, but also exhibits top-quality heating performance for rapid-heating applications. The saturation temperature of ITO/mica FTH can reach over 830 °C with an ultrafast thermal response shorter than 3 s. This high-speed response is primarily attributed to the high heat-transfer coefficient and low thickness of the mica substrate. As a thin-film rapid-annealing technique, the ITO/mica FTH can provide a robust platform for the integration of functional devices, which allows avenues toward realizing more efficient and cost-effective materials and device-manufacturing routes.

[1] A. Queraltó, M. de la Mata, J. Arbiol, X. Obradors, and T. Puig, Disentangling epitaxial growth mechanisms of solution derived functional oxide thin films, Adv. Mater. Interfaces **3**, 1600392 (2016).

[2] C. Li, Z. Wang, F. Li, Z. Rao, W. Huang, Z. Shen, S. Ke, and L. Shu, Large flexoelectric response in PMN-PT ceramics through composition design, Appl. Phys. Lett. **115**, 142901 (2019).

[3] Y. Yao, Z. Huang, P. Xie, S. D. Lacey, R. J. Jacob, H. Xie, F. Chen, A. Nie, T. Pu, M. Rehwoldt, D. Yu, M. R. Zachariah, C. Wang, R. Shahbazian-Yassar, J. Li, and L. B. Hu, Carbothermal shock synthesis of high-entropy-alloy nanoparticles, Science **359**, 1489 (2018).

[4] D. X. Luong, K. V. Bets, W. A. Algozeeb, M. G. Stanford, C. Kittrell, W. Chen, R. V. Salvatierra, M. Ren, E. A. McHugh, P. A. Advincula, Z. Wang, M. Bhatt, H. Guo, V. Mancevski, R. Shahsavari, B. Yakobson, and J. M. Tour, Gram-scale bottom-up flash graphene synthesis, Nature **577**, 647 (2020).

[5] M. G. Stanford, K. V. Bets, D. X. Luong, P. A. Advincula, W. Chen, J. T. Li, Z. Wang, E. A. McHugh, W. A. Algozeeb, B. Yakobson, and J. M. Tour, Flash graphene morphologies, ACS Nano **14**, 13691 (2020).

[6] W. Chen, Z. Wang, K. V. Bets, D. X. Luong, M. Ren, M. G. Stanford, E. A. McHugh, W. A. Algozeeb, H. Guo, G. Gao, B. Deng, J. Chen, J. T. Li, W. T. Carsten, B. Yakobson, and J. M. Tour, Millisecond conversion of metastable 2D materials by flash joule heating, ACS Nano **15**, 1282 (2021).

[7] C. Wang, *et al.*, A general method to synthesize and sinter bulk ceramics in seconds, Science **368**, 521 (2020).

[8] M. Patel, J. H. Seo, S. Kim, T. T. Nguyen, M. Kumar, J. Yun, and J. Kim, Photovoltaic-driven transparent heater of ZnO-coated silver nanowire networks for self-functional remote power system, J. Power Sources **491**, 229578 (2021).

[9] Y. J. Ke, J. W. Chen, C. J. Lin, S. C. Wang, Y. Zhou, J. Yin, P. S. Lee, and Y. Long, Smart windows: Electro-, thermo-, mechano-, photochromics, and beyond, Adv. Energy Mater. **9**, 1902066 (2019).

[10] S. J. Choi, S. J. Kim, J. S. Jang, J. H. Lee, and I. D. Kim, Silver nanowire embedded colorless polyimide heater for wearable chemical sensors: Improved reversible reaction kinetics of optically reduced graphene oxide, Small **12**, 5826 (2016).

[11] Y. Khan, A. E. Ostfeld, C. M. Lochner, A. Pierre, and A. C. Arias, Monitoring of vital signs with flexible and wearable medical devices, Adv. Mater. **28**, 4373 (2016).

[12] T. Wang, J. J. Wang, J. He, C. G. Wu, W. B. Luo, Y. Shuai, W. L. Zhang, X. C. Chen, J. Zhang, and J. Lin, A comprehensive study of a micro-channel heat sink using integrated thin-film temperature sensors, Sensor **18**, 299 (2018).

[13] H. B. Lee, W. Y. Jin, M. M. Ovhal, N. Kumar, and J. W. Kang, Flexible transparent conducting electrodes based on metal meshes for organic optoelectronic device applications: A review, J. Mater. Chem. C **7**, 1087 (2019).

[14] M. Li, S. L. Ji, J. Pan, H. Wu, L. Zhong, Q. Wang, F. D. Li, and G. H. Li, Infrared response of self-heating VO$_2$ nanoparticles film based on Ag nanowires heater, J. Mater. Chem. A **2**, 20470 (2014).

[15] H. Kim, M. Seo, J. W. Kim, D. K. Kwon, S. E. Choi, J. W. Kim, and J. M. Myoung, Highly stretchable and wearable thermotherapy pad with micropatterned thermochromic display based on Ag nanowire–single-walled carbon nanotube composite, Adv. Funct. Mater. **29**, 1901061 (2019).

[16] V. B. Nam, J. Shin, A. Choi, H. Choi, S. H. Ko, and D. Lee, High-Temperature, thin, flexible and transparent Ni-based heaters patterned by laser-induced reductive sintering on colorless polyimide, J. Mater. Chem. C **9**, 5652 (2021).

[17] S. Ji, J. Park, Y. Jo, Y. B. Kim, J. Jang, S. K. Kim, S. Jeong, and J. U. Park, Haze-free transparent electrodes using metal nanofibers with carbon shells for high-temperature stability, Appl. Surf. Sci. **483**, 1101 (2019).

[18] S. Ke, J. Xie, C. Chen, P. Lin, X. Zeng, L. Shu, L. Fei, Y. Wang, M. Ye, and D. Wang, Van der Waals epitaxy of Al-doped ZnO film on mica as a flexible transparent heater with ultrafast thermal response, Appl. Phys. Lett. **112**, 031905 (2018).

[19] Y. Bitla, C. Chen, H. Lee, T. Do, C. Ma, L. Qui, C. Huang, W. Wu, L. Chang, P. Chiu, and Y. H. Chu, Oxide heteroepitaxy for flexible optoelectronics, ACS Appl. Mater. Interfaces **8**, 32401 (2016).

[20] See the Supplemental Material at http://link.aps.org/supplemental/10.1103/PhysRevApplied.17.044049 for experimental configuration, XRD analysis of ITO/mica, heating profile of an ITO/glass heater, the surface emissivity of ITO

and mica, defogging test of ITO/mica, and PFM of HZO thin films.

[21] Y. H. Chu, Van der waals oxide heteroepitaxy, npj Quantum Mater. **2**, 67 (2017).

[22] J. Xie, Y. Bi, M. Ye, Z. Rao, L. Shu, P. Lin, X. Zeng, and S. Ke, Epitaxial ultrathin Au films on transparent mica with oxide wetting layer applied to organic light-emitting devices, Appl. Phys. Lett. **114**, 081902 (2019).

[23] H. Zhou, J. Xie, M. Mai, J. Wang, X. Shen, S. Wang, L. Zhang, K. Kisslinger, H. Q. Wang, J. X. Zhang, Y. Li, J. Deng, S. Ke, and X. Zeng, High-Quality AZO/Au/AZO sandwich film with ultralow optical loss and resistivity for transparent flexible electrodes, ACS Appl. Mater. Interfaces **10**, 16160 (2018).

[24] S. Ke, C. Chen, N. Fu, H. Zhou, M. Ye, P. Lin, W. Yuan, X. Zeng, L. Chen, and H. Huang, Transparent indium Tin oxide electrodes on muscovite mica for high-temperature-processed flexible optoelectronic devices, ACS Appl. Mater. Interfaces **8**, 28406 (2016).

[25] M. Wu, K. Liu, W. Wang, Y. Sui, X. Bai, and E. Wang, Ultralong aligned single-walled carbon nanotubes on flexible fluorphlogopite mica for strain sensors, Nano Res. **5**, 443 (2012).

[26] H. Ohta, M. Orita, M. Hirano, H. Tanji, H. Kawazoe, and H. Hosono, Highly electrically conductive indium-tin-oxide thin films epitaxially grown on yttria-stabilized zirconia (100) by pulsed-laser deposition, Appl. Phys. Lett. **76**, 2740 (2000).

[27] H. Ohta, M. Orita, M. Hirano, and H. Hosono, Surface morphology and crystal quality of low resistive indium Tin oxide grown on yittria-stabilized zirconia, J. Appl. Phys. **91**, 3547 (2002).

[28] G. Haacke, New figure of merit for transparent conductors, J. Appl. Phys. **47**, 4086 (1976).

[29] S. Ray, R. Banerjee, N. Basu, A. Batabyal, and A. Barua, Properties of tin doped indium oxide thin films prepared by magnetron sputtering, J. Appl. Phys. **54**, 3497 (1983).

[30] L. Mogg, G. P. Hao, S. Zhang, C. Bacaksiz, Y. C. Zou, S. J. Haigh, F. M. Peeters, A. K. Geim, and M. Lozada-Hidalgo, Atomically thin micas as proton-conducting membranes, Nat. Nanotechnol. **14**, 962 (2019).

[31] J. Bae, S. Lim, G. Han, Y. Jo, D. Doung, E. Kim, S. Chae, T. Huy, N. V. Luan, and Y. Lee, Heat dissipation of transparent graphene defoggers, Adv. Funct. Mater. **22**, 4819 (2012).

[32] P. Liu, L. Liu, K. Jiang, and S. Fan, Carbon-nanotube-film microheater on a polyethylene terephthalate substrate and Its application in thermochromic displays, Small **7**, 732 (2011).

[33] S. Sorel, D. Bellet, and J. N. Coleman, Relationship between material properties and transparent heater performance for both bulk-like and percolative nanostructured networks, ACS Nano **8**, 4805 (2014).

[34] T. Sannicolo, M. Lagrange, A. Cabos, C. Celle, J. P. Simonato, and D. Bellet, Metallic nanowire-based transparent electrodes for next generation flexible devices: A review, Small **12**, 6052 (2016).

[35] C. Zhang, M. Giroux, T. A. Nour, and R. St-Gelais, Radiative Heat Transfer in Freestanding Silicon Nitride Membranes, Phys. Rev. Appl. **14**, 024072 (2020).

[36] S. L. Ji, W. W. He, K. Wang, Y. X. Ran, and C. H. Ye, Thermal response of transparent silver nanowire/PEDOT:PSS film heaters, Small **10**, 4951 (2014).

[37] J. Kang, H. Kim, K. S. Kim, S. K. Lee, S. Bae, J. H. Ahn, Y. J. Kim, J. B. Choi, and B. H. Hong, High-performance graphene-based transparent flexible heaters, Nano Lett. **11**, 5154 (2011).

[38] Y. D. He, H. L. Dong, Q. Meng, L. Jiang, W. Shao, L. F. He, and W. P. Hu, Mica, a potential two-dimensional-crystal gate insulator for organic field-effect transistors, Adv. Mater. **23**, 5502 (2011).

[39] E. H. Ko, H. J. Kim, S. J. Lee, J. H. Lee, and H. K. Kim, Nano-sized Ag inserted into ITO films prepared by continuous roll-to-roll sputtering for high-performance, flexible, transparent film heaters, RSC Adv. **6**, 46634 (2016).

[40] N. M. Gueye, A. Carella, R. Demadrille, and J. P. Simonato, All-Polymeric flexible transparent heaters, ACS Appl. Mater. Interfaces **9**, 27250 (2017).

[41] D. T. Papanastasiou, A. Schultheiss, D. Munoz-Rojas, C. Celle, A. Carella, J. P. Simonato, and D. Bellet, Transparent heaters: A review, Adv. Funct. Mater. **30**, 1910225 (2020).

[42] J. Jang, N. S. Parmar, W. K. Choi, and J. W. Choi, Rapid defrost transparent thin-film heater with flexibility and chemical stability, ACS Appl. Mater. Interfaces **12**, 38406 (2020).

[43] K. Sun, W. Zhou, X. Tang, Z. Huang, F. Luo, and D. Zhu, Effect of the heat treatment on The infrared emissivity of indium tin oxide (ITO) films, Appl. Surf. Sci. **257**, 9639 (2011).

[44] S. H. Lim and H. K. Kim, Deposition rate effect on optical and electrical properties of thermally evaporated $WO_{3-x}/Ag/WO_{3-x}$ multilayer electrode for transparent and flexible thin film heaters, Sci. Rep. **10**, 8357 (2020).

[45] S. Wang, Q. Ai, T. Q. Zou, C. Sun, and M. Xie, Analysis of radiation effect on thermal conductivity measurement of semi-transparent materials based on transient plane source method, Appl. Therm. Eng. **177**, 115457 (2020).

[46] K. D. M. Rao and G. Kulkarni, A highly crystalline single Au wire network as a high temperature transparent heater, Nanoscale **6**, 5645 (2014).

[47] C. Celle, C. Mayousse, E. Moreau, H. Basti, A. Carella, and J. P. Simonato, Highly flexible transparent film heaters based on random networks of silver nanowires, Nano Res. **5**, 427 (2012).

[48] T. Kim, Y. W. Kim, H. S. Lee, H. Kim, W. S. Yang, and K. Suh, Uniformly interconnected silver-nanowire networks for transparent film heaters, Adv. Funct. Mater. **23**, 1250 (2013).

[49] H. Wang, S. Lin, D. Zu, J. Song, Z. Liu, Li Lei, C. Jia, X. Bai, J. Liu, Z. Li, D. Wang, Y. Huang, M. Fang, M. Lei, B. Li, and H. Wu, Direct blow spinning of flexible and transparent Ag nanofiber heater, Adv. Mater. Technol. **4**, 1900045 (2019).

[50] X. Zhu, Q. Xu, H. Li, M. Liu, Z. Li, K. Yang, J. Zhao, L. Qian, Z. Peng, G. Zhang, J. Yang, F. Wang, D. Li, and H. Lan, Fabrication of high-performance silver mesh for transparent glass heaters via electric-field-driven microscale 3D printing and UV-assisted microtransfer, Adv. Mater. **31**, 1902479 (2019).

[51] Z. Ma, S. Kang, J. Ma, L. Sao, A. Wei, C. Liang, J. Gu, B. Yang, D. Dong, L. Wei, and Z. Ji, High-performance and rapid-response electrical heaters based on ultraflexible, heat-resistant, and mechanically strong aramid nanofiber/Ag nanowire nanocomposite papers, ACS Nano **13**, 7578 (2019).

[52] T. Y. Zhang, H. M. Zhao, D. Y. Wang, Q. Wang, Y. Pang, N. Q. Deng, H. W. Cao, Y. Yang, and T. L. Ren, A super flexible and custom-shaped graphene heater, Nanoscale **9**, 14357 (2017).

[53] T. L. Chen, D. S. Ghosh, M. Marchena, J. Osmond, and V. Pruneri, Nanopatterned graphene on a polymer substrate by a direct peel-off technique, ACS Appl. Mater. Interfaces **7**, 5938 (2015).

[54] K. Huang, J. Liu, L. Tan, J. Zuo, and L. Fu, Ultrahigh temperature graphene molecular heater, Adv. Mater. Interfaces **5**, 1701299 (2018).

[55] Y. H. Yoon, J. W. Song, D. Kim, J. Kim, J. K. Park, S. K. Oh, and C. S. Han, Transparent film heater using single-walled carbon nanotubes, Adv. Mater. **19**, 4284 (2007).

[56] T. J. Kang, T. Kim, S. M. Seo, Y. J. Park, and Y. H. Kim, Transparent flexible heater based on hybrid of carbon nanotubes and silver nanowires, Carbon **49**, 1087 (2011).

[57] D. Jung, D. Kim, K. Lee, L. Overzet, and G. Lee, Transparent film heaters using multi-walled carbon nanotube sheets, Sens. Actuators, A **199**, 176 (2013).

[58] H. Jang, S. K. Jeon, and S. Nahm, The manufacture of a transparent film heater by spinning multi-walled carbon nanotubes, Carbon **49**, 111 (2011).

[59] D. Kim, L. Zhu, D. J. Jeong, K. Chun, Y. Y. Bang, S. R. Kim, J. H. Kim, and S. K. Oh, Transparent flexible heater based on hybrid of carbon nanotubes and silver nanowires, Carbon **63**, 530 (2013).

[60] C. Hudaya, J. H. Park, W. C. Choi, and J. K. Lee, Characteristics of fluorine-doped tin oxide as a transparent heater on PET prepared by ECR-MOCVD, ECS Trans. **53**, 161 (2013).

[61] B. D. Ahn, S. H. Oh, D. U. Hong, D. H. Shin, A. Moujoud, and H. J. Kim, Transparent Ga-doped zinc oxide-based window heaters fabricated by pulsed laser deposition, J. Cryst. Growth **310**, 3303 (2008).

[62] Y. Zhang, J. Nie, J. M. Chan, and J. Luo, Probing the densification mechanisms during flash sintering of ZnO, Acta Mater. **125**, 465 (2017).

[63] J. Matthews, Growth of face-centered-cubic metals on sodium chloride substrates, J. Vac. Sci. Technol. **3**, 133 (1966).

[64] D. Ji, S. Cai, T. Paudel, H. Sun, C. Zhang, L. Han, Y. Wei, Y. Zhang, M. Gu, Y. Zhang, W. Gao, H. Huyan, W. Guo, D. Wu, Z. Gu, E. Tsymbal, P. Wang, Y. Nie, and X. Pan, Freestanding crystalline oxide perovskites down to the monolayer limit, Nature **570**, 87 (2019).

[65] D. Lu, D. Beak, S. Hong, L. Kourkoutis, Y. Hikita, and H. Y. Hwang, Synthesis of freestanding single-crystal perovskite films and heterostructures by etching of sacrificial water-soluble layers, Nat. Mater. **15**, 1255 (2016).

[66] S. Wong, T. Sands, and N. Cheung, Damage-free separation of GaN thin films from sapphire substrates, Appl. Phys. Lett. **72**, 599 (1998).

[67] M. Lorenz, H. Hochmuth, D. Natusch, H. Börner, G. Lippold, and K. Kreher, Large-area double-side pulsed laser deposition of $YBa_2Cu_3O_{7-x}$ thin films on 3-in. sapphire wafers, Appl. Phys. Lett. **68**, 3332 (1996).

[68] H. Yang, W. Wang, Z. Liu, and G. Li, Homogeneous epitaxial growth of AlN single-crystalline films on 2 inch-diameter Si (111) substrates by pulsed laser deposition, J. Phys. D: Appl. Phys. **46**, 105101 (2013).

[69] C. Varanasi, K. Leedy, D. Tomich, and G. Subramanyam, Large area $Ba_{1-x}Sr_xTiO_3$ thin films for microwave applications deposited by pulsed laser ablation, Thin Solid Films **517**, 2878 (2009).

[70] S. Boughaba, M. Islam, J. P. McCaffrey, G. I. Sproule, and M. J. Graham, Ultrathin Ta_2O_5 films produced by large-area pulsed laser deposition, Thin Solid Films **371**, 119 (2000).